SANDIA REPORT
SAND2018-10917
Unlimited Release
Printed September 2018

Mechanics of Gold Nanoparticle Superlattices at High Hydrostatic Pressure

Ishan Srivastava, Brandon L. Peters, J. Matthew D. Lane, Hongyou Fan, and Gary S. Grest
Sandia National Laboratories, Albuquerque, NM 87185, USA

K. Michael Salerno
U.S. Army Research Laboratory, Aberdeen Proving Ground, MD 21005, USA

Prepared by
Sandia National Laboratories
Albuquerque, New Mexico 87185 and Livermore, California 94550

Sandia National Laboratories is a multimission laboratory managed and operated by National Technology and Engineering Solutions of Sandia, LLC, a wholly owned subsidiary of Honeywell International, Inc., for the U.S. Department of Energy's National Nuclear Security Administration under contract DE-NA0003525.


Sandia National Laboratories

Issued by Sandia National Laboratories, operated for the United States Department of Energy by National Technology and Engineering Solutions of Sandia, LLC.

Available to DOE and DOE contractors from

U.S. Department of Energy
Office of Scientific and Technical Information
P.O. Box 62
Oak Ridge, TN 37831

Telephone: (865) 576-8401
Facsimile: (865) 576-5728
E-Mail: reports@osti.gov
Online ordering: http://www.osti.gov/scitech

Available to the public from

U.S. Department of Commerce
National Technical Information Service
5301 Shawnee Rd
Alexandria, VA 22312

Telephone: (800) 553-6847
Facsimile: (703) 605-6900
E-Mail: orders@ntis.gov
Online order: https://classic.ntis.gov/help/order-methods/

SAND2018-10917
Printed September 2018
Unlimited Release

Mechanics of Gold Nanoparticle Superlattices at High Hydrostatic Pressure

Ishan Srivastava, Brandon L. Peters, J. Matthew D. Lane, Hongyou Fan, and Gary S. Grest
Sandia National Laboratories
P. O. Box 5800
Albuquerque, New Mexico 87185 USA

K. Michael Salerno
U.S. Army Research Laboratory
Aberdeen Proving Ground, Maryland 21005 USA

Abstract

Pressure-driven assembly of ligand-grafted gold nanoparticle superlattices is a promising approach for fabricating gold nanostructures, such as nanowires and nanosheets. However, optimizing this fabrication method requires an understanding of the mechanics of their complex hierarchical assemblies at high pressures. We use molecular dynamics simulations to characterize the response of alkanethiol-grafted gold nanoparticle superlattices to applied hydrostatic pressures up to 15 GPa, and demonstrate that the internal mechanics significantly depend on ligand length. At low pressures, intrinsic voids govern the mechanics of pressure-induced compaction, and the dynamics of collapse of these voids under pressure depend significantly on ligand length. These microstructural observations correlate well with the observed trends in bulk modulus and elastic constants. For the shortest ligands at high pressures, coating failure leads to gold core-core contact, an augur of irreversible response and eventual sintering. This behavior was unexpected under hydrostatic loading, and was only observed for the shortest ligands.

ACKNOWLEDGMENTS

This work was supported by the Sandia Laboratory Directed Research and Development Program. This work was performed, in part, at the Center for Integrated Nanotechnologies, an Office of Science User Facility operated for the U.S. Department of Energy (DOE) Office of Science. Sandia National Laboratories is a multimission laboratory managed and operated by National Technology and Engineering Solutions of Sandia, LLC, a wholly owned subsidiary of Honeywell International, Inc., for the U.S. Department of Energy's National Nuclear Security Administration under Contract No. DE-NA0003525.

TABLE OF CONTENTS

FIGURES

NOMENCLATURE

Abbreviation	Definition
NPSL	Nanoparticle superlattice
fcc	Face centered cubic
GPa	Giga Pascal

1. INTRODUCTION

Nanoparticle superlattices (NPSLs) are highly-ordered hierarchical structures assembled from passivated nanoparticles. They have wide-ranging applications in plasmonics,[1–3] photonics,[4] catalysis[5] and gas separation[6] technologies. They possess remarkable mechanical properties, as demonstrated in 2D nanoparticle membranes[7–10] and 3D nanoparticle superlattices,[11–13] which makes them attractive in their potential applications. Particularly, NPSLs exhibit unusual optical properties that are tunable based on the size and shape of constitutive nanoparticles as well as the geometry of the superlattice. Recently, Li et al.[3] have demonstrated that modulating the applied pressure on NPSLs provides a convenient approach to tune their geometry, and thereby reversibly control their optical properties. However, optimizing such pressure-based methods requires a detailed understanding of the mechanical response of NPSLs to external stress.

Recent experiments and simulations have demonstrated the possibility of transforming 3D NPSLs into functional low-dimensional nanostructures, such as nanowires and nanosheets, by subjecting them to a large external stress, both in quasi-static loading and superfast dynamic compression.[3,13–15] The mechanics of such transformations, however, are not entirely established. For example, it has been suggested that the quasi-static transformation of NPSLs into nanowires occurs as a result of a combination of applied hydrostatic pressure and deviatoric stress on the superlattice.[3,13,16] Furthermore, it is desirable to reduce the operating hydrostatic pressures and deviatoric stresses by modulating ligand morphology in order to make the fabrication process more scalable. However, the dependence of such pressures and stresses on the morphology of grafted ligands is unknown. A comprehensive investigation of the internal mechanics of NSPLs at high external pressures—for various ligand morphologies—provides a rational starting point towards optimizing these stress driven nanofabrication methods.

The structure and dynamics of ligand-grafted nanoparticles has been a subject of several computational investigations. Early work has characterized the structure of ligand-grafted nanoparticles,[17] and many subsequent studies have sought to understand their dynamics in solution,[18–20] their aggregation and assembly into superstructures[21,22] such as superlattices,[23] and the mechanical properties of their assemblies.[24] Simulations have also identified the role of temperature, relative size of gold cores and ligands, and ligand end-group functionalization on the structure of grafted ligands,[25–30] and its correlation with the effective interaction between grafted nanoparticles.[27,30,31] It is, therefore, apparent that the structure of grafted ligands in NPSLs significantly controls their bulk mechanical response to external loading.

In this work we use molecular dynamics simulations to characterize the bulk mechanics of alkanethiol-grafted gold NPSLs that are compressed to high hydrostatic pressures. We correlate their bulk mechanics to the evolution of ligand and void space microstructure with increasing applied pressure, and observe them to be significantly dependent on the length of the grafted ligands. For the shortest simulated ligands with six carbon atoms, we find unexpected evidence of irreversible gold core-core contacts at high hydrostatic pressures. Lastly, we discuss the implications of these findings on designing stress-driven nanofabrication methods for transforming 3D gold NPSLs into low-dimensional nanostructures such as gold nanowires and nanosheets.

2. RESULTS AND DISCUSSION

2.1. Gold Nanoparticle Superlattice

The hierarchical design of gold NPSLs is comprised of an alkanethiol-grafted gold nanoparticle as the basic building block of a *fcc* superlattice. Bare gold nanoparticles were constructed by carving 5.9 nm diameter spheres from *fcc* gold crystal, which were then annealed and cooled at ambient temperature to create nearly spherical nanoparticles such as shown in Fig. 1(a). A uniform coating of alkanethiol ($C_nH_{2n+1}S$) ligands was grafted onto the surface of bare gold nanoparticles, as shown in Fig. 1(b). To study the effect of ligand length, gold NPSLs were constructed with three different alkanethiol ligands corresponding to 6, 12 and 18 carbon atoms. For the case of ligands with 12 carbon atoms, three ligand grafting densities were also analyzed: 4.7, 4.2 and 3.8 ligands/nm^2. 4.7 ligands/nm^2 corresponds to a full coverage density as observed in experiments.[32,33]

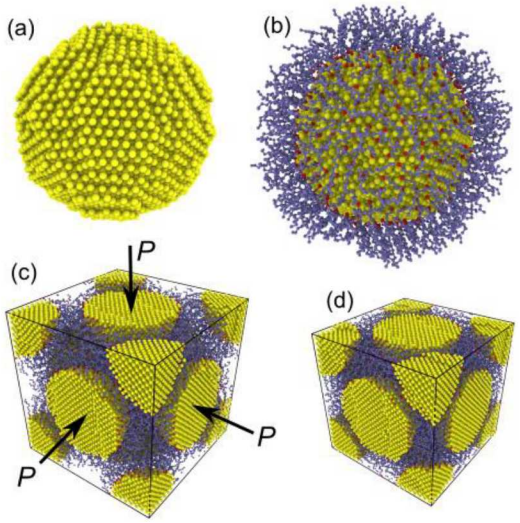

Figure 1. (a) Bare gold nanoparticle of 5.9 nm diameter (6662 atoms), cut from a bulk *fcc* gold lattice. (b) Gold nanoparticle grafted with $C_{12}H_{25}S$ ligands at a coverage of 4.7 chains/nm^2 (red: sulfur atoms, purple: carbon atoms, and yellow: gold atoms). (c) *fcc* unit cell of the ($C_{12}H_{25}S$)-grafted nanoparticle superlattice at ambient pressure P =10^{-4} GPa. Black arrows represent the application of an increasing pressure P to the superlattice. Black lines represent the 3D periodic cell boundaries. (d) *fcc* unit cell of the superlattice at a pressure P =15 GPa.

The alkanethiol-grafted gold nanoparticles were assembled into a *fcc* superlattice, and equilibrated at ambient conditions. Past simulations[13] and experiments[14–16] have demonstrated that *fcc* is the most stable structure for gold NPSLs. In the present simulations, we constructed gold NPSLs with 108 nanoparticles. Additionally, gold NPSLs consisting of 4 nanoparticles—i.e., the smallest structural unit needed to define a fcc superlattice—were also studied. Fig. 1(c) shows the image of a *fcc* superlattice consisting of 4 nanoparticles, which was equilibrated at ambient conditions. No significant deviations in the mechanical properties were observed between gold NPSLs constructed from 4 and 108 nanoparticles. Periodic boundary conditions were imposed to simulate the bulk behavior of the superlattice. Detailed simulation methodology including details of interatomic potentials is described in Materials and Methods section.

2.2 Pressure Compression

Gold NPSLs, equilibrated at ambient conditions, were volumetrically compressed to 15 GPa by ramping up the hydrostatic pressure at a rate of 1 GPa per nanosecond using NPT molecular dynamics with isotropic constraints on the deformation of the simulation cell. Fig. 1(d) shows the configuration of a gold NPSL depicted in Fig. 1(c), which was compressed to P = 15 GPa. The *fcc*

superlattice structure remained undistorted even at the highest simulated pressure for all ligand lengths and coverage densities.

Ligand length has a significant effect on average nanoparticle spacing d, with longer ligands resulting in higher d at all pressures, as show in Fig. 2(a). Ligand grafting density has only a moderate effect on nanoparticle spacing, and a denser grafting results in moderately higher d, as shown in Fig. 2(b). For the shortest ligand, the relative decrease in the average nanoparticle spacing upon compression is higher than the case of longer ligands, as seen by the variation of d/d_0 is inset of Fig. 2(a). Ligand grafting density has a small effect on d/d_0, and higher grafting density exhibits a slightly larger relative decrease in d with pressure, seen in the inset of Fig. 2(b). As seen in Figs. 2(a) and 2(b), d reduces rapidly at low pressures, and this is followed by a slow reduction at high pressures. Here d_o is nanoparticle spacing at 10^{-4} GPa. The rapid reduction in d at low pressures is attributed to affine volumetric compaction of the microstructure, which is accompanied by a collapse of the internal voids. At high pressures, a slower reduction in d with pressure results from the deformation of ligands as neighboring gold cores are pushed against one another in response to the applied pressure.

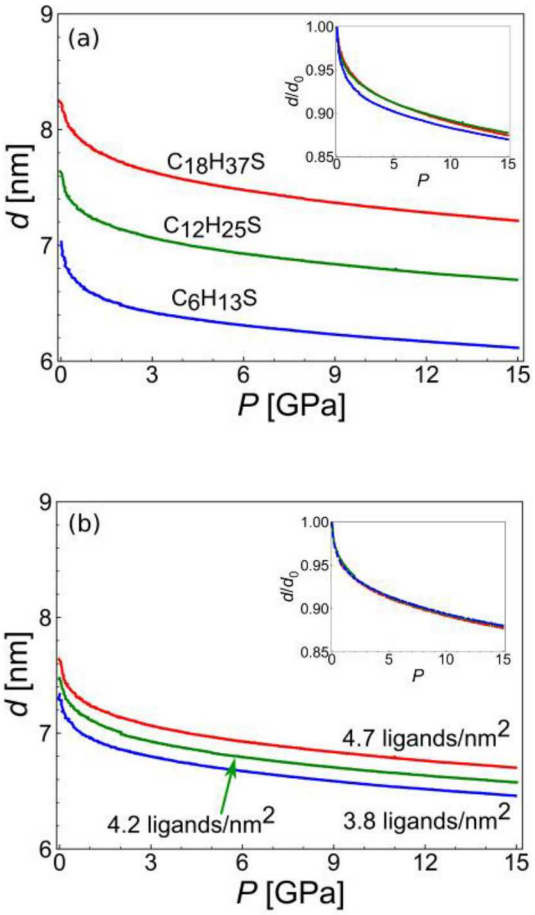

Figure 2. Average (center-to-center) separation d between adjacent nanoparticles in the *fcc* superlattice as a function of applied pressure for (a) varying ligand lengths at the maximum ligand coverage of 4.7 ligands/nm^2, and (b) varying coverage for $C_{12}H_{25}S$ ligands. From top to bottom, the curves correspond to a ligand coverage of 4.7, 4.2, and 3.8 ligands/nm^2. The insets in (a) and (b) show d/d_0 as a function of pressure, where d_0 is the inter-particle separation at ambient pressure P=10^{-4} GPa.

2.3 Elastic Moduli

To characterize the mechanics of *fcc* gold NPSLs at high pressures, we compute the bulk modulus K and two elastic moduli C_{11} and C_{12} of gold NPSLs at various values of applied pressure. The pressure-dependent bulk modulus was calculated by two different methods: (i) using the definition $K(P) = -V\frac{\partial P}{\partial V}$, bulk modulus is computed from the local derivative of pressure-volume evolution during pressure ramp simulations; and (ii) at discrete values of applied pressure, the unit cell is volumetrically compressed (within linear response regime), and bulk modulus is extracted from the resultant evolution of stress. A variation of method two, with uniaxial deformation of the unit cell at constant volume, was used to extract C_{11} and C_{12}. The methodology is elaborated in the Materials and Methods section.

Gold NPSLs with the shortest ligands have the largest bulk modulus, while the ones with the longest ligands have the smallest bulk modulus at all pressures, as shown in Fig. 3(a). This is expected because the longest ligand superlattice has the largest volume fraction of soft polymeric matter that is significantly more compressible that metallic gold. The bulk moduli calculated using method one (continuous lines) and method two (scatter points) at all pressures are equivalent, and this is demonstrative of rate-independence in elastic moduli calculations. This was further verified by compressing gold NPSLs at ten time slower pressure ramp rate, i.e., 0.1 GPa/ns. No difference in the measured bulk modulus was observed.The elastic moduli C_{11} and C_{12} of gold NPSLs lie between 3 and 11 GPa at the lowest calculated pressures of 2 GPa, as shown in Fig. 3(b). These values are consistent with experimentally characterized elastic constants of various NPSLs,[12,34,35] and are also similar to elastic constants of polymer glasses, thereby indicating a dominant role of ligands in the mechanical response a low pressures. All elastic constants increase with applied pressure, and while C_{11} is greater than C_{12}, both are lower than K at all pressures. Unlike the observable dependence of K on ligand length, we do not observe a clear ligand-length dependence of C_{11} and C_{12} at low and medium applied pressures.

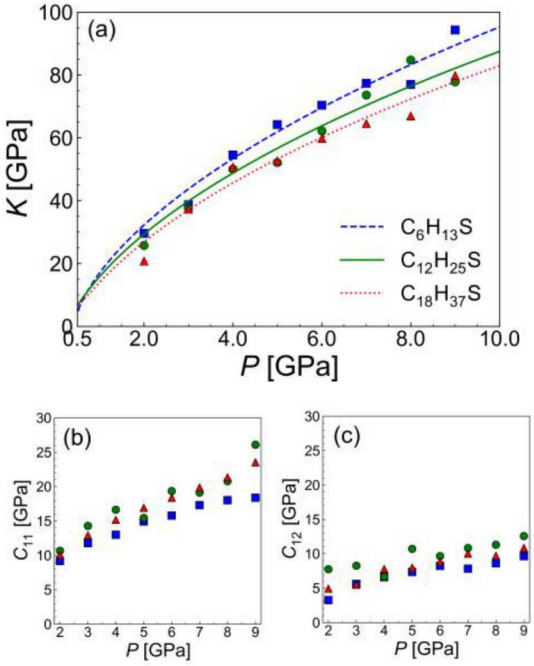

Figure 3. (a) Bulk modulus K as a function of applied pressure P. The solid lines represent K calculated from pressure-volume evolution during pressure ramp and symbols represent calculations from volumetric compression data at discrete values of pressure. Blue squares, green circles and red triangles correspond to ligand lengths with 6, 12, and 18 carbon atoms respectively. (b) and (c) Elastic constants C_{11} and C_{12} for the three

2.4 VOID COLLAPSE

Due to the spherical nature of bare and ligand-grafted nanoparticles, their *fcc* packing at ambient pressures is not completely dense and contains voids within the microstructure. The left column in Fig. 4(a) shows representative cross sections of the microstructure of gold NPSLs for three ligand lengths at ambient pressure, and the white space represents the void region. The total volume of voids is largest for the shortest ligand, and it is significantly reduced for longer ligands, which stretch out to occupy the void space. The total void volume is measured by constructing a surface mesh that divides the superlattice unit cell into a solid region containing ligands and gold cores, and a void region. The ratio of total void volume and total volume of superlattice unit cell is defined as the void volume fraction *v*. The space characterized as voids in the present simulations is typically occupied by a solvent in experiments[14–16] whose presence can influence the ligand microstructure and the bulk mechanics of the superlattice.

During early stages of compression at low pressures, void fraction decreases rapidly, as shown by the variation of *v* with pressure in Fig. 4(b). This occurs as a result of pressure induced affine motion of gold cores towards each other, and is accompanied by a rapid decrease in gold core

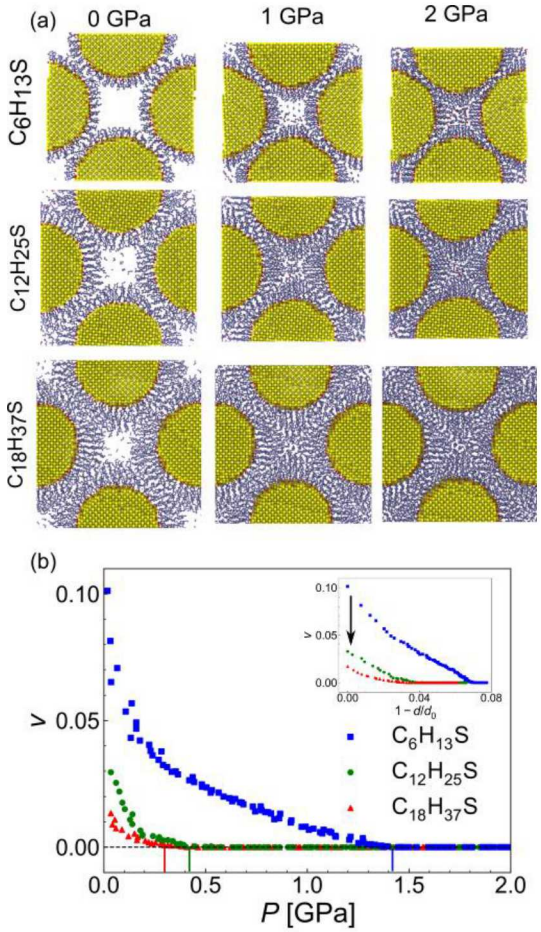

Figure 4: Evolution of void space in gold nanoparticle superlattices. (a) From top to bottom each row represents a cross-section of the microstructure along [001] and [010] *fcc* lattice directions in gold NPSLs grafted with alkanethiols containing 6, 12 and 18 carbon atoms at three different pressures: ambient (0 GPa), 1 GPa and 2 GPa from left to right respectively. (b) Void fraction *v* within the superlattice as a function of pressure for three ligand lengths. The solid vertical lines at the bottom of the graph denote the pressure at which voids completely collapse within the superlattice. The inset shows the variation of void fraction with the relative change in average gold core separation d from ambient separation d_0, and the arrow points towards data for increasing ligand length.

spacing as indicated by a concomitant increase in $(1-d/d_0)$ in the inset of Fig. 4(b). Gold NPSLs with shortest ligands exhibit largest relative reduction in void volume fraction during early stages of compression, and this is because the large initial void space provides least resistance to compression within superlattice microstructure. After rapid initial void space reduction, further removal of voids at higher pressures is not as rapid because ligands of neighboring gold nanoparticles resist additional deformation, as also seen by a slow reduction in d at higher pressures in Fig. 2. Upon approaching a certain threshold pressure, voids are completely collapsed within the microstructure, as shown in the middle and right panels of Fig. 4(a). The threshold pressure of complete void collapse depends significantly on ligand length, and is highest for shortest ligands as indicated in Fig. 4(b). In the presence of a typical solvent in experiments, a complete collapse of the voids is indicative of complete ejection of the solvent from the system.

2.5 Gold Core-Core Contacts

Typically, the presence of polymeric ligands prevents any contacts between gold cores upon hydrostatic compression, because the resultant volumetric compaction confines the ligands within the space between them, thus inhibiting their motion towards each other. In fact Li et al.[13] observed that a deviatoric stress (such as uniaxial stress), in addition to hydrostatic pressure, is necessary to drive contact formation and sintering between metal cores in nanoparticle superlattices. Fig. 5 shows cross-sections of *fcc* superlattices containing four nanoparticles at 15 GPa of applied pressure for three ligand lengths. For the cases of $C_{12}H_{25}S$ and $C_{18}H_{37}S$ ligands, the gold cores are well separated as expected, with the densely-packed ligands occupying the interstitial space. However, in the case of $C_6H_{13}S$ ligands, we find that the short ligands are able to deform enough to enable contact formation between gold cores even under hydrostatic pressure, as depicted by black ellipses in Fig. 5(a) and the accompanying

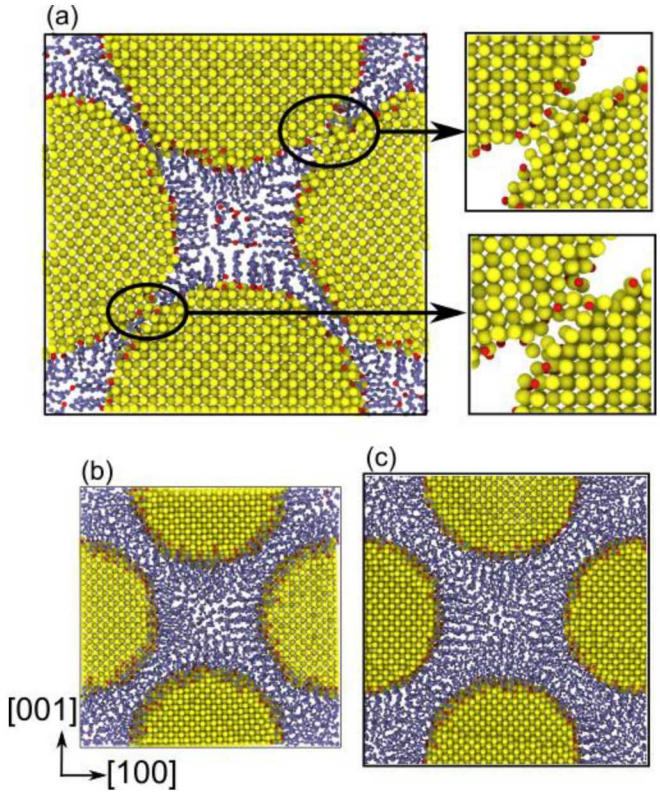

Figure 5. Cross-sections of gold nanoparticle superlattices with alkanethiol ligands containing (a) 6, (b) 12, and (c) 18 carbon atoms along [001] and [100] *fcc* lattice directions at an applied pressure of 15 GPa. The black ellipses highlight the contact region in (a), which is magnified to the right of the figure following the black arrows.

magnified images. In addition to ligand deformation, the contact formation is also aided by ligand migration away from the contact region.

We analyzed in further detail the phenomenon of gold core forming contacts by simulating *fcc* superlattice with 108 ($C_6H_{13}S$)-grafted gold nanoparticles. The superlattice was compressed from ambient to 15 GPa, then held at 15 GPa for 30 ns, followed by pressure reversal back to the ambient value. As the pressure was increased beyond 10 GPa, we found several (but not all) pairs of neighboring gold nanoparticles beginning to form contacts. While the system was held at the highest pressure of 15 GPa, we observed that some contacts grew in size to ~ 6 - 8 atoms wide The left and middle images Fig. 6(a) show two neighboring nanoparticles at ambient and after being held at the highest pressure. Fig. 6(b) shows the magnified contact region at the highest pressure. Prior simulations have demonstrated that contact formation between bare gold nanoparticles during sintering involves migration of surface gold atoms to reduce the total surface area, and therefore reduce the total free energy of the system.[36] Furthermore, this process occurs over a finite time that is dependent on nanoparticle size and temperature. Unlike bare nanoparticles, the contact region does not grow beyond a few gold atoms per contact over 30 ns of simulation time, and this could be attributed to the presence of ligands.

Upon reversing the pressure back to ambient, some of the contacts remained despite a reduction in their size. Fig. 6(c) shows the same magnified contact region in Fig. 6(b) after pressure reversal. The residual contact region contains a mix of gold atoms from both the neighboring nanoparticles, and we also observe the migration of some gold atoms from one nanoparticle surface to another. The persistence of gold core contacts is also reflected in the hysteresis of *fcc* superlattice volume V. In Fig. 6(d), the variation of V/V_0 with pressure exhibits an incomplete relaxation of the superlattice volume (about ~ 92 % of the original value) as the pressure is reversed back to ambient. Here V_0 is the volume at the start of the simulation. However the average spacing between all neighboring gold nanoparticles d exhibits little hysteresis, with its value relaxing back to ~98% of the original value d_0. This is because permanent contacts are not formed for all possible neighboring nanoparticles, but the ones that do form contribute to the hysteresis in the volume of the *fcc* superlattice. The observation of gold cores forming contacts at high pressure is observed even in the absence of any long-ranged interaction between them. A recent study has indicated that

significant long-range van der Waals attraction between gold cores can occur depending on the size of gold cores and the length of grafted ligands.[30] Such long-ranged interactions are expected to further drive irreversible sintering between the cores, and possibly at lower pressures.

3. CONCLUSIONS

We have demonstrated the effects of grafted ligand morphology on the mechanics and microstructure of gold NPSLs at high pressures. Ligand length significantly controls the elastic moduli at all values of applied pressure, and gold NPSLs with shorter ligands exhibit stiffer mechanical response. When the applied pressure on gold NPSLs is increased, the spacing between gold cores first decreases rapidly followed by a slower steady decrease, as the grafted ligands provide increased resistance to deformation at higher pressures. The void space in self-assembled gold NPSLs at ambient pressures governs the mechanical response at low pressures, and their removal upon densification is correlated with initial rapid decrease of the spacing between the gold cores. At very high applied pressures, we observe unexpected contact formation between neighboring gold cores that persist even when the pressure is reduced to its ambient value.

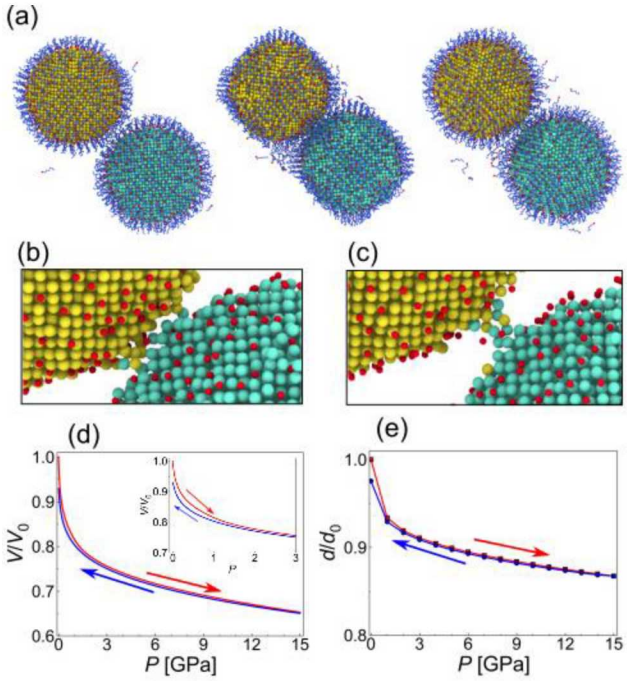

Figure 6. (a) Two neighboring nanoparticles within a gold nanoparticle superlattice with 108 ($C_6H_{13}S$)-grafted nanoparticles. From left to right: microstructure at ambient (0 GPa), 15 GPa, and ambient after pressure reversal. Gold atoms of the two nanoparticles are separately colored as gold and cyan. Carbon atoms and sulfur atoms are colored as red and blue respectively. (b) and (c) Microstructures of the magnified region of core-core contacts at 15 GPa and ambient after pressure reversal respectively. (d) Volume V of the *fcc* lattice supercell with 108 nanoparticles, normalized by the supercell volume $V_0 = 2.7 \times 10^4$ nm^3 at ambient, during pressure ramp-up and reversal in red and blue respectively (see arrows). The inset displays zoomed-in variation at low pressures. (e) Average inter-particle spacing d between all neighboring pairs of 108 nanoparticles, normalized by the average spacing d_0=7 nm at P=10^{-4} GPa, during pressure ramp-up and reversal in red and blue respectively (see arrows).

Our results imply that pressure-driven assembly of nanowires and nanosheets from NPSLs is likely to depend significantly on ligand morphology. Future work will directly explore the role of ligand properties on the limits of the non-hydrostatic loads required to induce sintering. Our focus, here, on hydrostatic stress states led to the surprising finding that sintering can occur even without deviatoric stresses. This finding and the pressure dependence of the elastic moduli point toward the need for further study of sintering and nanoparticle assembly under combinations of hydrostatic and deviatoric stress. We believe such a study could dramatically reduce pressures necessary for pressure-driven assembly (i.e. nanostructure fabrication).

4. MODEL AND METHOD

Gold nanoparticles are prepared by a procedure outlined in previous works.[9,18,27] The 5.9 nm gold nanoparticle studied here is cut from a gold fcc lattice and contains 6662 gold atoms. Au-Au atomic interaction is modeled by embedded atom method potential.[37] The temperature of the nanoparticle core is maintained at 300K for 1 ns, then raised to 800K for 1 ns to anneal the nanoparticle edges and corners, followed by cooling back to 300K for 1 ns. The heating and cooling of gold nanoparticle is simulated in a NVT ensemble with a temperature damping constant of 1 ps and a simulation time step of 1 fs.

The gold nanoparticle is then exposed to a gas of sulfur atoms, which adsorb on the surface of gold nanoparticles, thus describing the placement of thiol headgroup on the nanoparticle. During sulfur placement, interaction between Au and S atoms are modeled via Lennard-Jones parameters $\sigma_{S\text{-}S}$ = 4:64 Å and $\sigma_{S\text{-}Au}$ = 3:7 Å, and interaction strength $u_{S\text{-}S}$ = 5 kcal/mol and $u_{S\text{-}Au}$ = 10 kcal/mol. The interaction parameters govern the density of Au-S binding sites, and these parameters are chosen to reproduce experimental observations of alkanethiol grafting density of 4.7 ligands/nm^2.[32,33] For lower grafting densities corresponding to 4.2 and 3.8 ligands/nm^2, 10% and 20% respectively of the adsorbed S atoms on the gold nanoparticle surface are randomly removed.

Alkane ligands are initially attached to the thiol-headgroup binding sites such that they are oriented radially outward from the nanoparticle. The interaction between the atoms of alkanethiol ligands are modeled by optimized potential for liquid simulations—all-atom force field,[38] modified with an updated dihedral potential[39] and with non-bonded interactions modeled using an exponential-6 form.[40] Long-ranged electrostatic interactions are computed using particle-particle-particle-mesh method with a precision of 1 x10^{-5}.[41] The interaction between Au and S atoms is modeled with a Morse potential with parameters from Henz et al.,[42] which results in a binding strength that is consistent with reported values in the literature [43] The RESPA multi-step integrator[44] is used that integrates bond, angle, dihedral, van der Waals interactions, and direct interactions part of the electrostatic interactions, and time steps 2.0 fs for the k-space contribution to the long-range electrostatic interactions. All simulations are performed using LAMMPS molecular dynamics package.[45]

An *fcc* superlattice is constructed by placing as-prepared grafted nanoparticles on the *fcc* lattice sites, such that center-center spacing of neighboring nanoparticles is 8 nm, 9 nm and 11 nm for ligand lengths with 6, 12 and 18 carbon atoms respectively. Gold NPSLs are then volumetrically compressed at 300K using Langevin thermostat with a time constant of 1 ps such that the center-center spacing is reduced to ~ 6.8 nm, 7.3 nm and 7.5 nm for increasing ligand lengths. The compressed gold NPSLs are relaxed at 300K and 1 bar pressure for 4 ns in an NPT ensemble[46] with a temperature damping constant of 0.2 ps and pressure damping constant of 1.0 ps. The equilibrated gold NPSLs are then subjected to a constant-temperature pressure with pressure damping constant of 2.0 ps.

REFERENCES

1. Fan, J. A.; Wu, C.; Bao, K.; Bao, J.; Bardhan, R.; Halas, N. J.; Manoharan, V. N.; Nordlander, P.; Shvets, G.; Capasso, F. Self-assembled Plasmonic Nanoparticle Clusters. Science 2010, 328, 1135–1138.

2. Jones, M. R.; Osberg, K. D.; Macfarlane, R. J.; Langille, M. R.; Mirkin, C. A. Templated Techniques for the Synthesis and Assembly of Plasmonic Nanostructures. Chem. Rev. 2011, 111, 3736–3827.

3. Li, B.; Wen, X.; Li, R.; Wang, Z.; Clem, P. G.; Fan, H. Stress-induced Phase Transformation and Optical Coupling of Silver Nanoparticle Superlattices into Mechanically Stable Nanowires. Nat. Commun. 2014, 5, 4179.

4. Stebe, K. J.; Lewandowski, E.; Ghosh, M. Oriented Assembly of Metamaterials. Science 2009, 325, 159–160.

5. Bell, A. T. The Impact of Nanoscience on Heterogeneous Catalysis. Science 2003, 299, 1688–1691.

6. Bilchak, C. R.; Buenning, E.; Asai, M.; Zhang, K.; Durning, C. J.; Kumar, S. K.; Huang, Y.; Benicewicz, B. C.; Gidley, D. W.; Cheng, S. et al. Polymer-Grafted Nanoparticle Membranes with Controllable Free Volume. Macromolecules 2017, 50, 7111–7120.

7. He, J.; Kanjanaboos, P.; Frazer, N. L.; Weis, A.; Lin, X.-M.; Jaeger, H. M. Fabrication and Mechanical Properties of Large-Scale Freestanding Nanoparticle Membranes. Small 2010, 6, 1449–1456.

8. Mueggenburg, K. E.; Lin, X.-M.; Goldsmith, R. H.; Jaeger, H. M. Elastic Membranes of Close-packed Nanoparticle Arrays. Nat. Mater. 2007, 6, 656–660.

9. Salerno, K. M.; Bolintineanu, D. S.; Lane, J. M. D.; Grest, G. S. High Strength, Molecularly Thin Nanoparticle Membranes. Phys. Rev. Lett. 2014, 113, 258301.

10. Salerno, K. M.; Bolintineanu, D. S.; Lane, J. M. D.; Grest, G. S. Ligand Structure and Mechanical Properties of Single-Nanoparticle-Thick Membranes. Phys. Rev. E 2015, 91, 062403.

11. Landman, U.; Luedtke, W. D. Small is Different: Energetic, Structural, Thermal, and Mechanical Properties of Passivated Nanocluster Assemblies. Faraday Discuss. 2004, 125, 1–22.

12. Tam, E.; Podsiadlo, P.; Shevchenko, E.; Ogletree, D. F.; Delplancke-Ogletree, M.-P.; Ashby, P. D. Mechanical Properties of Face-Centered Cubic Supercrystals of Nanocrystals. Nano Lett. 2010, 10, 2363–2367.

13. Li, W.; Fan, H.; Li, J. Deviatoric Stress-driven Fusion of Nanoparticle Superlattices. Nano Lett. 2014, 14, 4951.

14. Li, B.; Bian, K.; Lane, J. M. D.; Salerno, K. M.; Grest, G. S.; Ao, T.; Hickman, R.; Wise, J.; Wang, Z.; Fan, H. Superfast Assembly and Synthesis of Gold Nanostructures using Nanosecond Low-Temperature Compression via Magnetic Pulsed Power. Nat. Commun. 2017, 8, 14778.

15. Wu, H.; Bai, F.; Sun, Z.; Haddad, R. E.; Boye, D. M.; Wang, Z.; Huang, J. Y.; Fan, H. Nanostructured Gold Architectures Formed through High Pressure-driven Sintering of Spherical Nanoparticle Arrays. J. Am. Chem. Soc. 2010, 132, 12826.

16. Wu, H.; Bai, F.; Sun, Z.; Haddad, R. E.; Boye, D. M.; Wang, Z.; Fan, H. Pressure-Driven Assembly of Spherical Nanoparticles and Formation of 1D-Nanostructure Arrays. Angew. Chem. 2010, 49, 8431–8434.

17. Luedtke, W.; Landman, U. Structure and Thermodynamics of Self-assembled Monolayers on Gold Nanocrystallites. J. Phys. Chem. B 1998, 102, 6566.

18. Lane, J. M. D.; Grest, G. S. Spontaneous Asymmetry of Coated Spherical Nanoparticles in Solution and at Liquid-Vapor Interfaces. Phys. Rev. Lett. 2010, 104, 235501.

19. Jayaraman, A. Polymer Grafted Nanoparticles: Effect of Chemical and Physica Heterogeneity in Polymer Grafts on Particle Assembly and Dispersion. J. Polym. Sci., Part B: Polym. Phys. 2013, 51, 524–534.

20. Van Lehn, R. C.; Alexander-Katz, A. Structure of Mixed-Monolayer-Protected Nanoparticles in Aqueous Salt Solution from Atomistic Molecular Dynamics Simulations. J. Phys. Chem. C 2013, 117, 20104–20115.

21. Akcora, P.; Liu, H.; Kumar, S. K.; Moll, J.; Li, Y.; Benicewicz, B. C.; Schadler, L. S.; Acehan, D.; Panagiotopoulos, A. Z.; Pryamitsyn, V. et al. Anisotropic Self-assembly of Spherical Polymer-grafted Nanoparticles. Nat. Mater. 2009, 8, 354–359.

22. Bozorgui, B.; Meng, D.; Kumar, S. K.; Chakravarty, C.; Cacciuto, A. Fluctuation-Drive Anisotropic Assembly in Nanoscale Systems. Nano Lett. 2013, 13, 2732–2737.

23. Kaushik, A. P.; Clancy, P. Explicit All-Atom Modeling of Realistically Sized Ligandcapped Nanocrystals. J. Chem. Phys. 2012, 136, 114702–13.

24. Liu, X. P.; Ni, Y.; He, L. H. Elastic Properties of Gold Supracrystals: Effects of Nanocrystal Size, Ligand Length, and Nanocrystallinity. J. Chem. Phys. 2016, 144, 144507–9.

25. Ghorai, P. K.; Glotzer, S. C. Molecular Dynamics Simulation Study of Self-Assembled Monolayers of Alkanethiol Surfactants on Spherical Gold Nanoparticles. J. Phys. Chem. C 2007, 111, 15857–15862.

26. Widmer-Cooper, A.; Geissler, P. Orientational Ordering of Passivating Ligands on CdS Nanorods in Solution Generates Strong Rod–Rod Interactions. Nano Lett. 2013, 14, 57–65.

27. Bolintineanu, D. S.; Lane, J. M. D.; Grest, G. S. Effects of Functional Groups and Ionization on the Structure of Alkanethiol-Coated Gold Nanoparticles. Langmuir 2014, 30, 11075–11085.

28. Salerno, K. M.; Ismail, A. E.; Lane, J. M. D.; Grest, G. S. Coating Thickness and Coverage Effects on the Forces between Silica Nanoparticles in Water. J. Chem. Phys. 2014, 140, 194904–9.

29. Widmer-Cooper, A.; Geissler, P. L. Ligand-Mediated Interactions between Nanoscale Surfaces Depend Sensitively and Nonlinearly on Temperature, Facet Dimensions, and Ligand Coverage. ACS Nano 2016, 10, 1877–1887.

30. Kister, T.; Monego, D.; Mulvaney, P.; Widmer-Cooper, A.; Kraus, T. Colloidal Stability of Apolar Nanoparticles: The Role of Particle Size and Ligand Shell Structure. ACS Nano 2018, 12, 5969–5977.

31. Silvera Batista, C. A.; Larson, R. G.; Kotov, N. A. Nonadditivity of Nanoparticle Interactions. Science 2015, 350, 1242477–1242477.

32. Strong, L.; Whitesides, G. M. Structures of Self-assembled Monolayer Films of Organosulfur Compounds Adsorbed on Gold Single Crystals: Electron Diffraction Studies. Langmuir 1988, 4, 546–558.

33. Woehrle, G. H.; Brown, L. O.; Hutchison, J. E. Thiol-Functionalized, 1.5-nm Gold Nanoparticles through Ligand Exchange Reactions: Scope and Mechanism of Ligand Exchange. J. Am. Chem. Soc. 2005, 127, 2172–2183.

34. Podsiadlo, P.; Krylova, G.; Lee, B.; Critchley, K.; Gosztola, D. J.; Talapin, D. V.; Ashby, P. D.; Shevchenko, E. V. The Role of Order, Nanocrystal Size, and Capping Ligands in the Collective Mechanical Response of Three-Dimensional Nanocrystal Solids. J. Am. Chem. Soc. 2010, 132, 8953–8960.

35. Yan, C.; Portalès, H.; Goubet, N.; Arfaoui, I.; Sirotkin, S.; Mermet, A.; Pileni, M.-P. Assessing the Relevance of Building Block Crystallinity for Tuning the Stiffness of Gold Nanocrystal Superlattices. Nanoscale 2013, 5, 9523–5.

36. Goudeli, E.; Pratsinis, S. E. Crystallinity Dynamics of Gold Nanoparticles during Sintering or Coalescence. AIChE J. 2015, 62, 589–598.

37. Foiles, S.; Baskes, M.; Daw, M. Embedded-Atom-Method Functions for the Fcc Metals Cu, Ag, Au, Ni, Pd, Pt, and their Alloys. Phys. Rev. B 1986, 33, 7983.

38. Jorgensen, W. L.; Maxwell, D. S.; Tirado-Rives, J. Development and Testing of the OPLS All-Atom Force Field on Conformational Energetics and Properties of Organic Liquids. J. Am. Chem. Soc. 1996, 118, 11225–11236.

39. Siu, S. W.; Pluhackova, K.; Böckmann, R. A. Optimization of the OPLS-AA Force Field for Long Hydrocarbons. J. Chem. Theory Comput. 2012, 8, 1459.

40. Borodin, O.; Smith, G. D. Development of Many-Body Polarizable Force Fields for Li- Battery Components: 1. Ether, Alkane, and Carbonate-Based Solvents. J. Phys. Chem. B 2006, 110, 6279–6292.

41. Hockney, R. W.; Eastwood, J. W. Computer Simulation Using Particles; Taylor and Francis: London, 1988.

42. Henz, B. J.; Hawa, T.; Zachariah, M. R. Mechano-Chemical Stability of Gold Nanoparticles Coated with Alkanethiolate SAMs. Langmuir 2008, 24, 773.

43. Jang, S. S.; Jang, Y. H.; Kim, Y.-H.; Goddard, W. A.; Flood, A. H.; Laursen, B. W.; Tseng, H.-R.; Stoddart, J. F.; Jeppesen, J. O.; Choi, J. W. et al. Structures and Properties of Self-Assembled Monolayers of Bistable [2]Rotaxanes on Au (111) Surfaces from Molecular Dynamics Simulations Validated with Experiment. J. Am. Chem. Soc. 2005, 127, 1563–1575.

44. Tuckerman, M.; Berne, B. J.; Martyna, G. J. Reversible Multiple Time Scale Molecular Dynamics. J. Chem. Phys. 1992, 97, 1990–2001.

45. Plimpton, S. Fast Parallel Algorithms for Short-Range Molecular Dynamics. J. Comp. Phys. 1995, 117, 1.

46. Martyna, G. J.; Tobias, D. J.; Klein, M. L. Constant Pressure Molecular Dynamics Algorithms. J. Chem. Phys. 1994, 101, 4177–4189.

DISTRIBUTION

4	Lawrence Livermore National Laboratory Attn: N. Dunipace (1) P.O. Box 808, MS L-795 Livermore, CA 94551-0808		
1	MS9054	Sarah Allendorf	8350
1	MS1315	Sean Hearne	1880
1	MS0351	William Seng	1190
1	MS0899	Technical Library	9536 (electronic copy)
1	MS0359	D. Chavez, LDRD Office	1911

Sandia National Laboratories